



Synthesis of 2,6-dimethylpyrazine by dehydrocyclization of aqueous glycerol and 1,2-propanediamine over Cu–Cr–O catalyst: Rationalization of active sites by pyridine and formic acid adsorbed IR studies

V. Krishna^{a,b}, G. Naresh^b, V. Vijay Kumar^b, R. Sarkari^b, A. Hari Padmasri^c, Akula Venugopal^{a,b,*}

^a Academy of Scientific and Innovative Research, India

^b Catalysis Laboratory, Inorganic and Physical Chemistry Division, CSIR-Indian Institute of Chemical Technology, Hyderabad, Telangana, 500 007, India

^c Department of Chemistry, University College for Women, Osmania University, Koti, Hyderabad, 500 095, Telangana, India

ARTICLE INFO

Article history:

Received 20 January 2016

Received in revised form 14 March 2016

Accepted 9 April 2016

Available online 12 April 2016

Keywords:

Dehydrocyclization

Aqueous glycerol

1,2-Propanediamine

2,6-Dimethylpyrazine

Pyridine–HCOOH-DRIFTS

CuO–CuCr₂O₄

XPS

NH₃-TPD

ABSTRACT

The mixed oxides of CuO–CuCr₂O₄ (Cu–Cr–O) with different Cu/Cr mole ratios were examined for synthesis of 2,6-dimethylpyrazine (2,6-DMP) by the utilization of aqueous glycerol in conjunction with 1,2-propanediamine (1,2-PDA). Influence of acid-base (both Bronsted and Lewis) sites on the product distribution is rationalized by pyridine and formic acid adsorbed Diffuse Reflectance Infrared Fourier Transform (DRIFT) spectroscopy. Pyridine adsorbed DRIFT spectra demonstrated relatively higher number Lewis acid sites on the chromium rich (Cu₁Cr₃) Cu–Cr–O than on copper rich (Cu₂Cr₁) Cu–Cr–O. The formic acid adsorbed IR spectra demonstrated strong basic sites attributed to the vibrational bands at 1584 cm^{−1} and 1677 cm^{−1} due to dissociative adsorption of formate species on Cu₂Cr₁ surface. The structure activity relationship is established with Cu metal surface area and the acid-base strengths of the Cu–Cr–O catalysts in the dehydrocyclization of glycerol and 1,2-PDA.

© 2016 Elsevier B.V. All rights reserved.

1. Introduction

Synthesis of fine chemicals, pharmaceutical drug intermediates and transportation fuels or fuel additives from bio-refineries utilizing renewable resources is a topic of interest [1]. With increasing expansion of biomass as raw material in general and biodiesel production in particular; glycerol is expected to become a major platform chemical for future bio-refineries [2]. In the context of biodiesel market, crude glycerol plays a very important role since it is the major by-product during biodiesel production, and also obtained as a by-product during other processes that use biomass as raw material [3]. Hence crude glycerol has become a building block that could serve as an important bio-refinery feedstock [4]. However, development of catalytic processes for the selective conversion of such glycerol into useful compounds is a challeng-

ing task. Plethora of literature is available on the transformation of bioglycerol into valuable chemicals. It is important to generate alternate fuels or chemicals from any renewable biomass. At the same time it is utmost important to safely dispose the by-products or convert them into useful compounds so as to make the alternative methods economically attractive for large scale operation. One of such methods is catalytic conversion of crude glycerol into 1,2-propanediol and 1,3-propanediol over supported noble metal catalysts at high H₂-pressures [5]. Currently these propanediols are produced from petroleum derivatives. 2-methylpyrazine (2-MP) an intermediate compound for the anti tuberculosis drug is being synthesized by cyclocondensation of ethylenediamine and 1,2-propanediol over Pd modified Zn–Cr–O catalyst [6]. We reported a mechanism first time on the selective synthesis of 2MP over Zn–Cr–O catalyst by effective utilization of crude glycerol [7]. It has been reported that nature and strength of acidic and basic sites on catalyst surface plays an important role on the catalytic activity and 2MP selectivity during the dehydrocyclization of crude glycerol and 1,2-propanediol [8–10]. This concept has been applied

* Corresponding author.

E-mail address: akula@iict.res.in (A. Venugopal).

for the synthesis of various alkylpyrazines with high selectivity and minimum by-products. Synthesis of alkylpyrazines is carried out by self condensation of α -amino carbonyl compounds and a combination of α -diketones with vicinal diamines followed by dehydrogenation [11]. Rizk et al. synthesized alkyl and substituted pyridines and pyrazines by intra molecular hydroamination in presence of *p*-toluenesulfonic acid [12]. However, these methods generate unusual by-products and afford a mixture of regional isomers [13]. Among several alkylpyrazines, 2,6-DMP is one of the valuable compounds for the production of various agro-chemicals, food flavoring agent and as a ligand for catalyst synthesis [14]. Vapor phase synthesis of alkylpyrazines is reported by Li et al. over Zn/Al₂O₃ catalyst using glycerol and 1,2-PDA [15]. Earlier we investigated the catalytic activity of M_xO_y-MCr₂O₄ (M = Mg, Fe, Co, Ni, Cu, Zn) mixed oxides for dehydrocyclization of crude glycerol and 1,2-propanediamine (1,2-PDA) for synthesis of 2,6-DMP [16]. The present study is aimed to define the role of acid-base sites and also the influence of surface Cu metal sites on the dehydrocyclization activity of Cu–Cr–O catalyst. Here we report a kinetic study on the influence of both Bronsted and Lewis (acid-base) sites on the dehydrocyclization activity and on the product selectivity. A detailed examination of the surface Bronsted and Lewis acid-base sites on the product distribution is emphasized by using pyridine and formic acid adsorbed IR spectroscopy combined with Cu metal surface area measured by pulse N₂O decomposition.

2. Materials and methods

2.1. Preparation of catalysts

The hydrotalcite precursors of Cu–Cr samples were prepared by a simple co-precipitation method using Cu(NO₃)₂·3H₂O and Cr(NO₃)₃·9H₂O (Sigma-Aldrich) with varied Cu/Cr mole ratios. In a typical procedure, required amount of Cu(NO₃)₂·6H₂O and Cr(NO₃)₃·9H₂O were dissolved in double distilled water and precipitated by using a mixture of 2 M NaOH + 1 M Na₂CO₃ at a constant pH of ~9.0. The resulted precipitate was washed several times with distilled water until the pH reached to 7.0. The cake was filtered, dried in air at 120 °C over night and subsequently calcined in static air at 500 °C for 5 h. The calcined samples are denoted as Cu_xCr_y where x and y indicate the number of moles of Cu and Cr present in the sample e.g. Cu₁Cr₂ represents Cu:Cr = 1:2 mol ratio. For comparison purpose both the bulk copper oxide (CuO) and chromium oxide (Cr₂O₃) were prepared using their respective nitrate salts under similar protocol which denoted as Cu₁Cr₀ and Cu₀Cr₁.

2.2. Characterization of catalysts

The thermal stability, dehydration and decomposition of the oven dried samples were examined by thermo gravimetric analysis (TGA) and differential thermal analysis (DTA) using a simultaneous thermo gravimetric analyzer (STA-409, NETZSCH) with a temperature programmed furnace. Specimens were heated in a temperature range from ambient to 750 °C in air at a ramping rate of 10 °C/min. The bulk and surface properties of the samples were analysed by BET-surface area, powder X-ray diffraction (XRD), Fourier transform infrared (FT-IR), Raman spectroscopy, temperature programmed reduction (H₂-TPR), X-ray photoelectron spectroscopy (XPS), atomic absorption spectroscopy (AAS), Carbon-hydrogen-nitrogen-sulphur (CHNS) analyzer and temperature programmed desorption of NH₃ (NH₃-TPD) techniques. The experimental conditions adopted for these analytical and spectroscopic methods were similar to what was reported by us earlier [10,16]. The AAS analysis of the samples revealed that there is no loss of metal during the preparation and activation (Table 1S). To investigate the nature

and strength of acid-base sites, pyridine and formic acid adsorbed FT-IR (Carry 660, Agilent Technologies) spectra were recorded at a resolution of 4 cm⁻¹. The experiments were performed *in-situ* using a purpose-made IR cell connected to a conventional vacuum-adsorption apparatus. In a typical method the sample powder was pressed into self-supporting wafers (density ~40 mg/cm²) under a pressure of 10⁵ Pa. After that, the sample was introduced in the IR cell. Firstly, the sample was pre-treated *in-situ* by heating in dynamic vacuum at a rate of 10 °C/min up to 400 °C/1 h. After cooling down to 150 °C, the spectrum (fresh) was collected in the DRIFT mode. Prior to pyridine adsorption, the samples were reduced using 5% H₂/Ar at 450 °C for 30 min and cooled to 150 °C in N₂ flow. Then the pyridine vapour was injected onto the sample in 3 pulses (total of ~5 mmol) followed by flushing the sample in N₂ for 1 h and the spectrum was recorded. The pyridine adsorbed DRIFT spectrum was subtracted with that of reduced form to obtain the vibrational bands due to pyridine-acid (Bronsted acid site: Py-H⁺ and Lewis acid site: Py-Mⁿ⁺) site interaction. In a similar protocol the H₂O (5 mmol) adsorbed and formic acid (~a dose of 5 mmol) adsorbed DRIFT spectra were collected in separate measurements. Finally, the spectra were quantified with Kubelka-Munk function. The UV-visible diffuse reflectance spectra were recorded on a UV-2600 SHIMADZU spectrophotometer in the range 200–800 nm. The Cu metal surface area was measured by N₂O decomposition at 80 °C. In a typical method about 50 mg of catalyst was reduced using 5% H₂/Ar at 450 °C for 30 min and subsequently the reactor was cooled in He gas flow (30 mL/min) from 450 °C to 80 °C. At this temperature, 0.5 mL of N₂O pulses were injected and the N₂O consumption was monitored using GC-TCD with Porapak N column. In this investigation, a surface copper density of 1.46 × 10¹⁹ atoms/m² was used for the copper metal area calculations. The measurements were replicated in order to avoid (in some case) the bulk oxidation of catalyst surface due to excess pulses and the N₂O pulses were limited to a maximum of 3–4 injections. For brevity some of the graphs were incorporated in the electronic supplementary information, unless otherwise mentioned.

2.3. Activity measurement

The vapour phase dehydrocyclization of aqueous glycerol and 1,2-PDA was carried out in a fixed bed down flow quartz reactor at atmospheric pressure in the temperature range of 300–425 °C under strict kinetic regime. Prior to the reaction the catalyst was reduced in 4.97% H₂ balance Ar at 450 °C for 3 h in some case the calcined sample was used as such for testing the activity. The reactor dimensions and the experimental conditions maintained for the activity studies were reported recently by us [16,ESI]. The liquid products were collected each hour in an ice-cold trap and analysed by gas chromatography (Shimadzu, GC-17A) using ZB-5 capillary column with FID. The carbon mass balance was ±1.0% unless otherwise stated. All the products were confirmed by GC-MS (QP5050A Shimadzu) using a ZB-5 capillary column with EI mode and NMR spectroscopy [ESI].

2.4. Calculations of conversion, rate and specific rate

$$\% \text{Conversion of 1, 2 - PDA} = \left[\frac{\text{moles}_{1,2\text{-PDAin}} - \text{moles}_{1,2\text{-PDAout}}}{\text{moles}_{1,2\text{-PDAin}}} \right] \times 100$$

$$\% \text{Conversion of Glycerol} = \left[\frac{\text{moles}_{\text{Gly.in}} - \text{moles}_{\text{Gly.out}}}{\text{moles}_{\text{Gly.in}}} \right] \times 100$$

$$\% \text{Selectivity} = \left[\frac{P_i/C_i}{\sum_i^n P_i/C_i} \right]$$

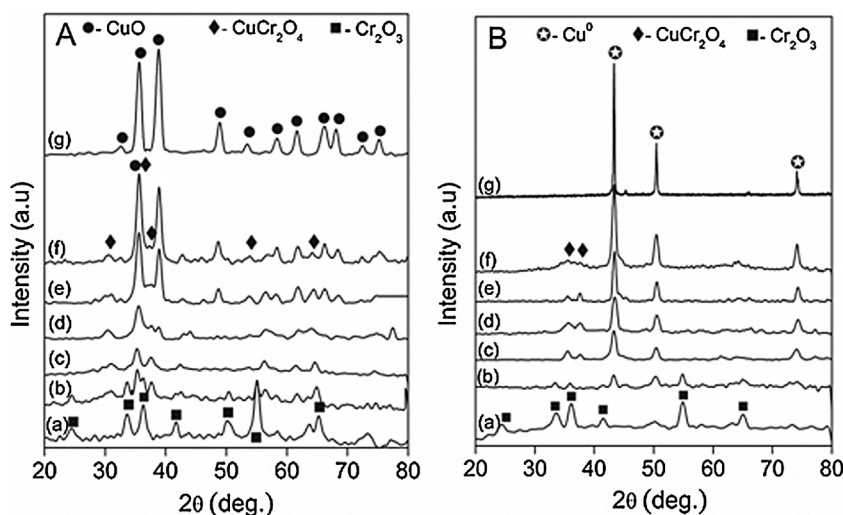


Fig. 1. XRD spectra of (A) calcined and (B) reduced Cu-Cr-O of (a) Cu_0Cr_1 (b) Cu_1Cr_3 (c) Cu_1Cr_2 (d) Cu_1Cr_1 (e) Cu_2Cr_1 (f) Cu_3Cr_1 and (g) Cu_1Cr_0 catalysts.

(where C_i and P_i are the stoichiometric factor and the product concentration, respectively).

$$\text{Yield}_{2,6\text{-DMP}} = \frac{[\text{Conv. Gly.} \times \text{Sel.}_{2,6\text{-DMP}}]}{100}$$

$$\text{Yield}_{6\text{-HMP}} = \frac{[\text{Conv. Gly.} \times \text{Sel.}_{6\text{-HMP}}]}{100}; \text{6-HMP: 6-hydroxymethyl-2-methylpyrazine}$$

Rate (r) is defined as

$$r_{2,6\text{-DMP}} = \left[\frac{(\text{Yield}_{2,6\text{-DMP}}) \times (1, 2 - \text{PDA} + \text{Glycerol}) \text{ flowrate}}{\text{Weight of the catalyst}} \right] \text{ moles g}_{\text{cat}}^{-1} \text{ s}^{-1}$$

$$r_{6\text{-HMP}} = \left[\frac{(\text{Yield}_{6\text{-HMP}}) \times (1, 2 - \text{PDA} + \text{Glycerol}) \text{ flowrate}}{\text{Weight of the catalyst}} \right] \text{ moles g}_{\text{cat}}^{-1} \text{ s}^{-1}$$

$$\text{TOF} = \frac{\text{Rate}}{\text{N}_2\text{O uptake}}$$

3. Results

3.1. XRD and TEM analysis

The XRD analysis of Cu-Cr (with varied mole ratios) demonstrated hydrotalcite (HT) like structure except for bulk CuO (Cu_1Cr_0) and bulk Cr_2O_3 (Cu_0Cr_1) samples (Fig. S1). The calcined Cu-Cr samples (Fig. 1A) indicated the decomposition of HT structure to form $\text{M}_x\text{O}_y\text{-M}'\text{Cr}_2\text{O}_4$ ($\text{M}' = \text{Cu}$; $\text{M}_x = \text{Cu}$ and/or Cr) mixed oxides. The CuCr_2O_4 phase is clearly visible in Fig. 1A (d–f). In case of Cu_1Cr_2 only CuCr_2O_4 spinel phase is observed [JCPDS # 72-1212]. However, the chromium rich Cu_1Cr_3 exhibited diffraction peaks attributed to Cr_2O_3 along with CuCr_2O_4 phase. An increase in copper ratio leads to an increase in the intensity of CuO and CuCr_2O_4 diffraction peaks. The Cu_1Cr_0 and Cu_0Cr_1 samples exhibited diffraction pattern of their respective bulk oxides CuO [JCPDS # 80-1268] and Cr_2O_3 [JCPDS # 85-0730] and all the binary Cu-Cr samples (Cu_3Cr_1 , Cu_2Cr_1 and Cu_1Cr_1) demonstrated a combination of CuO and CuCr_2O_4 phases. This indicates the formation of CuCr_2O_4 spinel which is energetically favourable in mixtures of Cu and Cr-oxides. The XRD spectra of reduced Cu-Cr samples (Fig. 1B) displayed strong diffraction lines corresponding to metallic copper [JCPDS # 04-0836] along with low intense peaks due to CuCr_2O_4 phase and

Cr_2O_3 in both Cu_0Cr_1 and Cu_1Cr_3 samples only. The sharp diffraction lines in reduced samples may probably be due to sintering of Cu that would cause an increase in its crystallite size [17,18]. The TEM images of calcined Cu_1Cr_0 , Cu_0Cr_1 and Cu_2Cr_1 samples (Fig. S2) are composed of irregular aggregates with different shape and

size. The mean particle size of Cu-Cr-O (Cu_2Cr_1) (Fig. S2a) is about 16.0 nm, whereas the bulk Cr_2O_3 (Fig. S2b) and CuO (Fig. S2c) oxides have an average particle size of 45.4 and 48.5 nm respectively.

3.2. H_2 -temperature programme reduction (H_2 -TPR) analysis

The H_2 -TPR patterns of calcined Cu-Cr (with varied mole ratios) are reported in Fig. 2. The bulk CuO (Cu_1Cr_0 ; Fig. 2a) showed a reduction peak (CuO to Cu^0) at T_{max} of 287 °C with a small shoulder at 380 °C. While introducing Cr, the TPR curves of Cu-Cr-O became broad with shoulder indicative of two stage reduction (Fig. 2b to 2f). The low temperature peak can be assigned to CuO and high temperature signal is attributed to partial reduction of copper chromate species. With decrease in Cu/Cr ratio the T_{max} shifted towards high temperature; suggesting the interaction between Cu and Cr species to form spinel structure. The outward diffusion of Cu^{2+} to form segregated CuO species may be difficult in presence of chromium ions due to mutual interaction between copper and chromium [19]. The bulk chromium oxide (Cu_0Cr_1) showed a reduction signal at 374 °C that can be ascribed to reduction of surface chromate Cr^{6+} species to Cr^{3+} [20]. The hydrogen consumption is decreased with an increase in chromium content and bulk CuO (Cu_1Cr_0) consumed the maximum hydrogen. It should be mentioned here that the complete reduction of chromium oxide to zero valence chromium is not possible under the TPR conditions adopted in this study [21]. Upon decreasing the Cu/Cr ratio, the BET-surface areas have increased; thus suggesting the contribution of chromium in enhancing the

Table 1
Physicochemical properties of Cu–CrO catalysts.

Catalyst	XRD phases	^a Crystalline size (nm)		^b BET-SA (m ² g ^{−1})	^c H ₂ uptake (μmol g ^{−1})	^d NH ₃ uptake		N ₂ O uptake μmol/g _{cat}
		CuO	CuCr ₂ O ₄			μmol/g	μmol/m ²	
Cu ₁ Cr ₀	CuO	16.8	nf	13.6	742.7	80.2	0.05	33.0
Cu ₃ Cr ₁	CuO, CuCr ₂ O ₄	16.8	10.6	17.6	565.7	170.1	0.09	45.8
Cu ₂ Cr ₁	CuO, CuCr ₂ O ₄	13.8	13.6	24.2	480.6	240.6	0.09	78.0
Cu ₁ Cr ₁	CuO, CuCr ₂ O ₄	11.4	14.1	20.6	313.4	380.0	0.18	50.7
Cu ₁ Cr ₂	CuCr ₂ O ₄	nf	15.9	21.3	227.1	400.3	0.18	46.6
Cu ₁ Cr ₃	CuCr ₂ O ₄ , Cr ₂ O ₃	12.6	17.3	20.4	146.0	470.5	0.23	28.9
Cu ₀ Cr ₁	Cr ₂ O ₃	16.8	nf	15.7	44.2	130.2	0.08	nd

nf: not found; nd: not determined.

^a Average crystallite size measured from XRD patterns of calcined Cu–Cr–O samples using Scherrer formula.

^b BET–surface areas of the calcined catalysts.

^c H₂ uptakes measured by TPR analysis calibrated with TPR of Ag₂O.

^d NH₃ uptakes measured by TPD of NH₃ of the reduced catalysts.

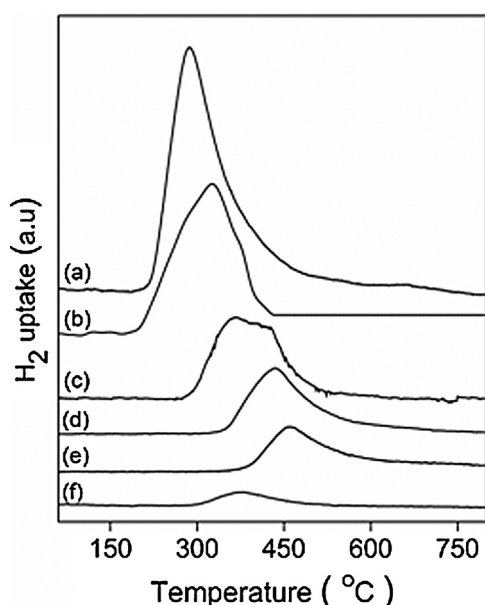


Fig. 2. H₂–TPR profiles of calcined (a) Cu₁Cr₀, (b) Cu₃Cr₁, (c) Cu₁Cr₁, (d) Cu₁Cr₂, (e) Cu₁Cr₃ and (f) Cu₀Cr₁ samples.

surface area of the Cu–Cr–O samples. The TPR analysis revealed a decrease in H₂ uptake with a decrease in Cu/Cr mole ratio (Table 1).

3.3. Raman spectroscopic and FTIR analysis of Cu–Cr–O

The Raman spectra of calcined Cu–Cr–O samples showed a band at 263 cm^{−1} that is assigned to A_g and 298, 633 cm^{−1} bands are B_g modes of CuO species (Fig. S3). All the Cu–Cr–O samples showed vibrational bands around 304 cm^{−1} (A_{1g}), 345 cm^{−1} (A_{1g}), 387 cm^{−1} (A_{1g}), 517 cm^{−1} (E_g), 541 cm^{−1} (E_g) and 602 cm^{−1} (F_{2g}) except Cu₁Cr₀ sample. Upon increasing the copper loading intensities of these peaks increased [22,23]. The calcined and reduced forms of Cu–Cr–O samples as analysed by FT-IR and their spectra are illustrated in Fig. 3. The broad vibrational bands (in both calcined and reduced) around 3450 cm^{−1} and 1630 cm^{−1} are ascribed to stretching and bending vibrations of coordinated water and surface hydroxyl groups [24,25]. The bands observed at 438, 543 and 602 cm^{−1} in Cu₁Cr₀ corresponds to Cu–O vibration in bulk CuO [26]. According to Waldron et al. and White et al., the high frequency band (614 cm^{−1}) is the feature of tetrahedral metal–O stretching vibration and the low frequency band (513 cm^{−1}) is due to the vibration of octahedral metal–O bond present in a spinel structure [27,28]. The Cu–Cr–O samples exhibited the bands at 513 cm^{−1} and 614 cm^{−1} that correspond to the stretching vibration of Cu–O–Cr

and Cr–O in CuCr₂O₄ [29]. These results are in good correlation with XRD data that depicted the formation of CuCr₂O₄. It is also evident that this band shows a blue shift with increase in chromium content. The vibrational bands observed around 570 and 630 cm^{−1} in bulk chromia (Fig. 3A (g)) originated from Cr–O vibration in crystalline Cr₂O₃ [30,31]. A band at 934 cm^{−1} is attributed to Cr=O stretching vibrations of mono and poly nuclear surface chromate species present in all Cu–Cr–O samples (Fig. 3A (b–g)) except in Cu₁Cr₀ [9,32]. These Cr=O linkages represent the high valence state of chromium, possibly due to Cr⁶⁺ as there is no evidence of any Cr⁵⁺; the other paramagnetic species in the ESR spectra of Cu–Cr–O (Fig. S4). The band which appeared around 1040 cm^{−1} is due to metal–O stretching vibration. The intensities of the vibrational bands due to CuCr₂O₄ spinel (510–620 cm^{−1}) are lowered after reduction; thus suggesting the reductive pre-treatment induces amorphous spinel structure and metallic copper sites. Absence of the vibrational band at 934 cm^{−1} is clearly evident in reduced samples (Fig. 3B) emphasizing the reduction of chromate to chromite species (Cr⁶⁺ to Cr³⁺). This observation is further supplemented by high temperature reduction signals in the TPR analysis of Cu–Cr–O samples (Fig. 2).

3.4. UV–vis DRS analysis

The UV–DRS spectra of calcined and reduced Cu–Cr samples are illustrated in Fig. S5. The calcined Cu–Cr–O samples demonstrated similar band positions with varied absorption intensities at 246–255 nm attributed to ligand to metal charge transfer (O^{2−}–Cu²⁺) in octahedral coordination of Cu²⁺ (Fig. S5A). This absorption band is associated with minor population of dispersed Cu²⁺ species. The broad band in 360–800 nm region is overlapped absorptions arising from variety of Cu²⁺ species [33]. The absorption signals at 250–270 nm and 350–370 nm are assigned to dispersed copper and chromium (mainly Cr⁶⁺) species probably interacting together [21]. The spectrum of bulk chromia (Cu₀Cr₁) displayed absorption maxima at 270, 365, 456 and 604 nm characteristic bands of chromium in multiple oxidation states although only Cr₂O₃ phase is detected from XRD analysis (Fig. 1A). We believe that some portion of chromium exists in an oxidation state >3 and <6 (Cu²⁺–O–Cr^{x+} where 3 ≤ x ≤ 6) i.e. copper chromate species in the unreduced form. The band intensity at 250–270 nm slightly decreased in reduced samples compared to their fresh form (Fig. S5B). The absorption band in the region 350–370 nm disappeared suggesting the conversion of Cr⁶⁺ to Cr³⁺ after reduction [34].

3.5. X-ray photoelectron spectroscopy (XPS)

The XPS analysis of calcined samples with varied Cu/Cr mole ratios (Cu₃Cr₁, Cu₂Cr₁, Cu₁Cr₁, Cu₁Cr₂ and Cu₁Cr₃) are reported

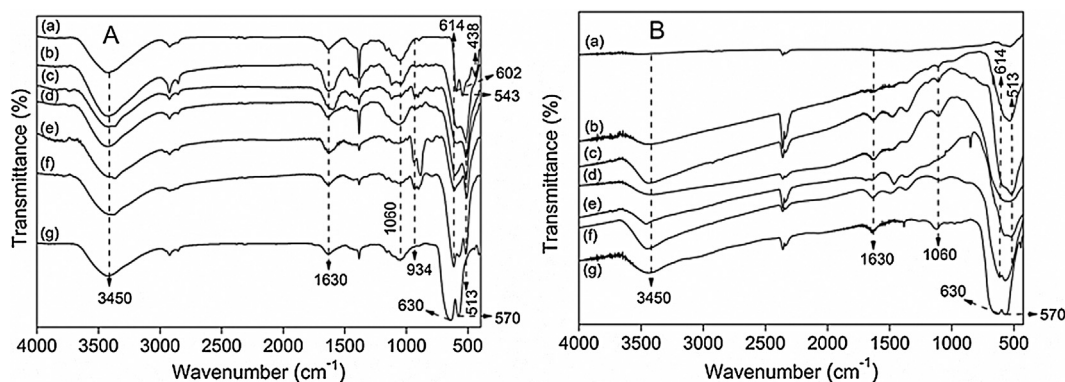


Fig. 3. IR spectra of (A) calcined and (B) reduced Cu–Cr–O (a) Cu_1Cr_0 (b) Cu_3Cr_1 (c) Cu_2Cr_1 (d) Cu_1Cr_1 (e) Cu_1Cr_2 (f) Cu_1Cr_3 and (g) Cu_0Cr_1 samples.

in Fig. 4. The XPS lines located at binding energy (BE) 934.4 and 954.0 eV assigned to $\text{Cu } 2p_{3/2}$ and $\text{Cu } 2p_{1/2}$ respectively are an indication of Cu^{2+} in the near surface region (Fig. 4a). Presence of satellite peak at 942 eV from the high energy component is an evidence for the existence Cu^{2+} species [35]. At higher chromium (Cu_1Cr_2 and Cu_1Cr_3) loading the $\text{Cu } 2p$ signal slightly shifted towards higher B.E (Fig. 4a). This may be caused by the change in chemical environment around copper ions with the rearrangement of cation distribution in spinel sub-lattice with the increase in chromium content [36]. The $\text{Cr } 2p_{3/2}$ peak shows a clear asymmetry and is resolved into two peaks at 576.4 and 578.3 eV (Fig. 4b). These peaks are assigned to Cr^{3+} and Cr^{6+} respectively [37]. On the contrary TPR measurements showed decreased H_2 uptakes with increase in Cu/Cr mole ratio. The shift in XPS signal to higher BE can be possible while the chromium cation is surrounded by higher number of oxygen ligands. Sloczynski et al. [38] reported that surface of chromium containing spinel oxides are enriched with Cr^{6+} and were located at surface only. This shoulder peak is very weak in copper rich (Cu_2Cr_1) sample. The broad O 1s signal is an indication of signal contributions from multiple oxygen species in the near surface region (Fig. 4c). The intense main oxygen peaks have shoulders at higher binding energies, which can be resolved into two components with peaks around 531.6 and 530.2 eV respectively. The two peaks of O 1s are distinguished as $\text{O}_{\text{surface}}$ and $\text{O}_{\text{lattice}}$ while $\text{O}_{\text{surface}}$ has a binding energy about 1.4 eV higher than that of $\text{O}_{\text{lattice}}$. The $\text{O}_{\text{surface}}$ peaks are associated with variety of species such as surface chemisorbed oxygen, hydroxyl and oxygen ions in low coordination situation and/or oxygen-containing surface contamination, while the signal at low binding energy could be lattice oxygen [39–41].

3.6. NH_3 -TPD analysis

The NH_3 uptakes on reduced Cu–Cr–O samples estimated by TPD (Fig. S6) are reported in Table 1. The bulk CuO and Cr_2O_3 possess lower acidity than Cu–Cr–O mixed oxides. Addition of chromium showed significant differences in the desorption profiles. The Cu_1Cr_3 sample exhibited higher acidity than other Cu–Cr–O samples and bulk oxides (Table 1).

3.7. Activity measurements

Dehydrocyclization of aqueous glycerol and 1,2-PDA is carried out over Cu–Cr–O samples (with varied Cu/Cr mole ratios) and the results are reported in Table 2. Bulk Cr_2O_3 (Cu_0Cr_1) showed lower conversion of both glycerol and 1,2-PDA compared to bulk CuO . In contrast the mixed oxide component of Cu–Cr–O samples demonstrated very high conversion than their individual oxides. Interestingly, selectivity of 2,6-dimethylpiperazine (2,6-

DMPip $\sim 43.2\%$) is higher on bulk Cr_2O_3 than other samples. High proportion of 2,6-DMPip can be explained by the primary reaction step i.e. dehydration of glycerol to hydroxyacetone (HA) and subsequent condensation of HA with 1,2-PDA to produce 2,6-DMPip. It appears that the rate of dehydrogenation of 2,6-DMPip to generate 2,6-DMP may be slow on Cr_2O_3 compared to CuO . On the contrary 2,6-DMP selectivity is quite high over bulk CuO (Cu_1Cr_0) compared to bulk Cr_2O_3 (Cu_0Cr_1). Lack of sufficient number of basic sites on Cr_2O_3 surface may be a reason for the decrease in the dehydrogenation of 2,6-DMPip to 2,6-DMP. The bulk CuO (Cu_1Cr_0) demonstrated lower acidity (Table 1) than the bulk Cr_2O_3 (Cu_0Cr_1). Regardless of acidity, the Cu_1Cr_0 showed a rate of 2,6-DMP $\sim 0.66 \mu\text{mol g}_{\text{cat}}^{-1} \text{s}^{-1}$ which is approximately an order of magnitude higher than the Cu_0Cr_1 ($0.06 \mu\text{mol g}_{\text{cat}}^{-1} \text{s}^{-1}$). Conversely the rate of 2,6-DMPip is very high over Cu_0Cr_1 compared to Cu_1Cr_0 . In the comparative analysis the 2,6-DMP rate is very high on Cu_2Cr_1 than bulk oxides and other Cu–Cr–O catalysts. Using a simulated crude glycerol mixture that contained KOH and methanol (expected from the bio-diesel plants); the Cu_2Cr_1 showed promising activity than the Cu_1Cr_3 catalyst (Table 1). From this data it can be inferred that both copper and chromium sites are desirable for dehydrocyclization of aqueous glycerol and 1,2-PDA as the individual bulk oxides were inferior compared to the Cu–Cr–O catalysts. Upon using a crude bio-glycerol obtained from biodiesel production plant using Jatropha oil (Jatropha Curcas) that contained about 11 wt% of glycerol, 4 wt% KOH, 5 wt% NaCl and 80 wt% H_2O ; it is found that both the glycerol and 1,2-PDA conversions decreased drastically. Under these conditions the rate of 2,6-DMP decreased by an order of magnitude. The rapid fall of 2,6-DMP formation is attributed to large amount of KOH present in the crude bio-glycerol (Table 2). It is known that dehydrocyclization of glycerol and ethylenediamine requires a pair of acid-base sites on the catalyst surface [8]. Formation of 2,6-dimethylpyrazine is mainly due to dehydration of glycerol to hydroxyacetone (HA) followed by cyclocondensation of HA with 1,2-PDA to produce 2,6-DMP via Schiff base mechanism [Scheme S1]. The nature and strength of Brønsted and Lewis (both acid and basic sites on Cu–Cr–O) sites is examined by pyridine (as probe for acid) and formic acid (as probe for basic sites) adsorbed DRIFT spectra in order to rationalize their influence on 2,6-DMP rates over a Cu-rich and a Cr-rich Cu–Cr–O samples and the data is compared with the bulk CuO and Cr_2O_3 samples.

4. Discussion

Dehydrocyclization of aqueous glycerol and 1,2-PDA is examined over Cu_2Cr_1 sample with and without reductive pre-treatment and the activity data is reported in Table S2. The unreduced Cu_2Cr_1 exhibited poor 2,6-DMP rate than its reduced form. About four times higher 2,6-DMP rate ($3.83 \times 10^{-6} \text{mol g}_{\text{cat}}^{-1} \text{s}^{-1}$)

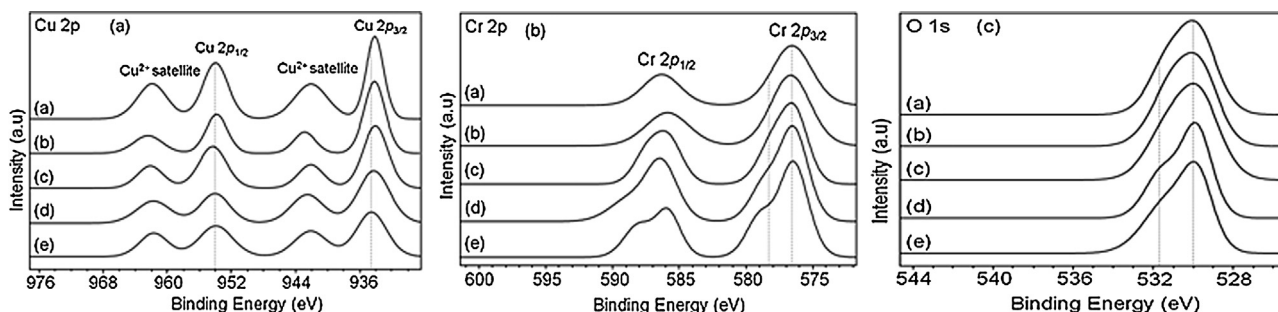


Fig. 4. X-ray photoelectron spectra of calcined samples. (a) Cu 2p (b) Cr 2p and (c) O 1s spectra of the Cu–Cr–O (a) Cu_3Cr_1 (b) Cu_2Cr_1 (c) Cu_1Cr_1 (d) Cu_1Cr_2 and (e) Cu_1Cr_3 catalysts. Fig. 5: Rate of 2,6-dimethylpyrazine with varying Cu/Cr mole ratio.

Table 2

Dehydrocyclization of aqueous glycerol and 1,2-PDA over reduced Cu–Cr–O catalysts at a reaction temperature = 350 °C and feed flow rate = 2 mL/h (10 wt% glycerol in H_2O ; glycerol:1,2-PDA = 1).

Catalyst	Conversion (%)		Selectivity (%)				^b Rate/ $10^{-8} \text{ mol (g}_{\text{cat}})^{-1} \text{ s}^{-1}$		
	X_{glycerol}	$X_{1,2\text{-PDA}}$	$S_{2,6\text{-DMP}}$	$S_{6\text{-HMP}}$	$S_{2,6\text{-DMPip}}$	^a S_{others}	2,6-DMP	6-HMP	2,6-DMPip
Cu_1Cr_0	12.8	13.3	91.2	2.4	1.2	5.2	66.1	1.7	0.8
Cu_3Cr_1	27.8	28.3	90.1	3.8	2.2	3.8	141.9	5.9	3.4
Cu_2Cr_1	74.5	76.4	90.8	6.0	1.1	2.1	383.3	25.3	4.6
Cu_1Cr_1	53.1	57.3	80.4	6.2	5.0	8.4	241.9	18.5	15.4
Cu_1Cr_2	36.4	38.3	80.0	5.7	7.2	7.8	165.0	11.7	14.2
Cu_1Cr_3	10.4	12.0	71.3	8.4	12.1	8.2	42.0	4.9	7.0
Cu_0Cr_1	3.8	4.5	30.0	16.2	43.2	10.6	6.4	3.4	9.1
^c Cu_2Cr_1	31.2	33.4	74.7	13.2	3.7	8.4	132.0	23.3	6.5
^d Cu_2Cr_1	9.3	10.1	71.3	13.2	4.3	11.2	37.5	6.9	2.2

^a Others include 2,5-DMP and 5-HMP.

^b Rate of 2,6-DMP, 6-HMP and 2,6-DMPip measured with respect to glycerol conversion and their selectivity.

^c Crude bio-glycerol composition: 10 mmol glycerol + 10 mmol 1,2-PDA + 0.2 μmol KOH + 0.3 mmol CH_3OH + 200 mmol H_2O .

^d Crude bio-glycerol received during biodiesel production from Jatropha oil (Jatropha Curcas) that contained about 11 wt% of glycerol, 4 wt% KOH, 5 wt% NaCl and ~80 wt% H_2O .

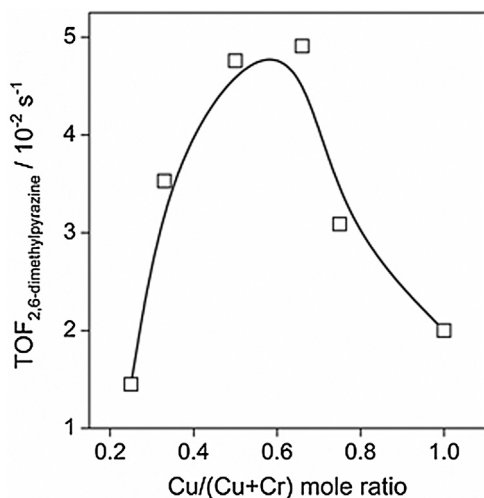


Fig. 5. Rate of 2,6-dimethylpyrazine with varying Cu/Cr mole ratio.

is observed when compared to calcined unreduced catalyst ($0.81 \times 10^{-6} \text{ mol g}_{\text{cat}}^{-1} \text{ s}^{-1}$). It is important to note that 2,6-DMP selectivity is excellent although the conversion is poor with unreduced (Cu_2Cr_1) catalyst. The higher dehydrocyclization rate on reduced sample revealed the importance of metallic copper. This is further evidenced from Fig. 5 that showed a direct correlation between Cu metal surface area and the rate of 2,6-DMP.

As aforementioned, there are structural differences between reduced and unreduced Cu_2Cr_1 . The unreduced sample showed Cu^{2+} and chromium as mono and poly nuclear chromates (Fig. 3A; band at 934 cm^{-1} due to higher oxidation of chromium >3 and <6)

likely to be in the form of $\text{Cu}[\text{Cr}^{3+}\text{Cr}^{x+}]_x\text{O}_4$ ($3 < x < 6$) species. On the contrary the reduced Cu_2Cr_1 manifested the presence of metallic copper and Cr^{3+} species (Fig. 3B). It is also found from XPS analysis that the intensity of the shoulder peak at 579.2 eV due to Cr^{6+} gradually decreased with decrease in chromium loading (Fig. 4b).

Upon increasing the GHSV, both glycerol and 1,2-PDA conversions decreased drastically, obviously due to short contact time (Table S3). However, selectivity of 2,6-DMP is maintained about 80% even at very high GHSV. These results pointed out the selective dehydrocyclization activity of Cu–Cr–O catalysts i.e. composed of CuO – CuCr_2O_4 mixed oxides. The NH_3 -TPD results gave information on the strength and number of acidic sites present on the catalyst surface (Table 1). It has been emphasized that bi-functional characteristics (both acidic and basic sites) on mixed metal oxides are important for dehydrocyclization reaction to occur [8,9]. The surface acidic sites on Cu–Cr–O are active for dehydration of glycerol and basic sites promote the dehydrogenation of glycerol. Formation of 2,6-dimethylpyrazine is mainly due to dehydration of glycerol to hydroxyacetone (HA) followed by cyclocondensation of HA with 1,2-PDA to produce 2,6-DMP via Schiff base mechanism [16]. Hence the nature of acidic sites on Cu–Cr–O is investigated by pyridine adsorbed and the basic sites are analysed by formic acid adsorbed DRIFT spectroscopy.

The nature of Brønsted and/or Lewis acid sites are distinguished by pyridine adsorbed DRIFT spectra over Cu_2Cr_1 and Cu_1Cr_3 samples (Fig. 6). The pyridine adsorbed IR spectra displayed bands at 1605 and 1438 – 1445 cm^{-1} that are assigned to Lewis acid sites and the band at 1480 cm^{-1} indicated the existence of both Brønsted and Lewis sites [42]. The IR band appeared at 1563 cm^{-1} has been ascribed to pyridine adsorbed on Brønsted acid sites (Fig. 6) i.e. shifted towards higher wavenumber ($+23 \text{ cm}^{-1}$) which is quite contrast to the Lewis band that is shifted to lower wavenumber

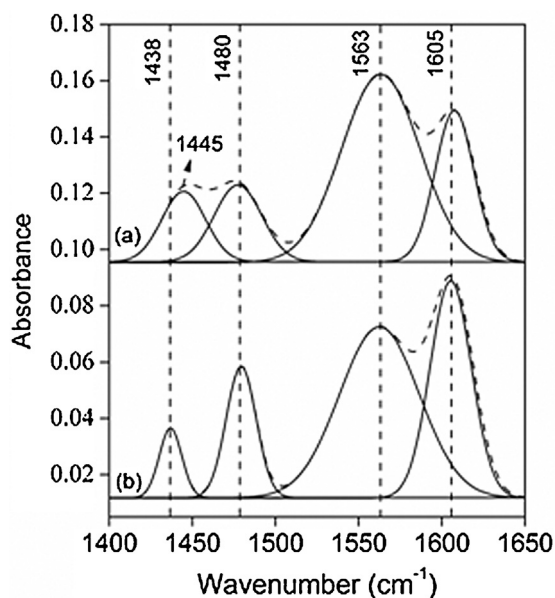


Fig. 6. IR spectra of pyridine adsorbed on (a) Cu_1Cr_3 and (b) Cu_2Cr_1 catalysts.

1438 cm^{-1} [43]. The peak shift in both the samples assigned to both Lewis and Bronsted sites is because of Fermi resonance as the pyridine adsorption on Lewis site usually shows the band at 1450 cm^{-1} and Bronsted at 1540 cm^{-1} . On the other hand this shift is less pronounced (-5 cm^{-1}) as the pyridine adsorbed acidic Lewis band appeared at 1445 cm^{-1} in chromium rich Cu_1Cr_3 (Fig. 6a). Quite contrast to this Cu_2Cr_1 exhibited the vibrational band at 1438 cm^{-1} , a shift of about -12 cm^{-1} is observed. Both the samples exhibited a red shift with respect to Lewis acid sites and no appreciable difference in vibrational bands due to pyridine adsorbed on Bronsted acid sites.

The comparative analysis revealed that (Fig. 6a and b) both Cu_1Cr_3 and Cu_2Cr_1 samples exhibited higher number of Bronsted acid sites (BAS) and very low population of Lewis acid sites (LAS) on their surface. The relative ratios of $\text{BAS}_{\text{Cu}_2\text{Cr}_1}:\text{BAS}_{\text{Cu}_1\text{Cr}_3}=0.9$, discernible from the high concentration of chromium in Cu_1Cr_3 than in Cu_2Cr_1 ; considering excess chromium present on the Cu_1Cr_3 surface. Evidence to this fact is further observed from the near surface compositions obtained by XPS analysis that showed (Table S4) $\text{Cr}_{\text{Cu}_2\text{Cr}_1}:\text{Cr}_{\text{Cu}_1\text{Cr}_3}=0.52$. The ratios of the normalized relative intensities of bands due to Lewis (LAS) and Bronsted acid sites (BAS) appearing in the regions at $1438\text{--}1445\text{ cm}^{-1}$ and 1563 cm^{-1} measured (in order to compare the acid strengths of Cu_2Cr_1 and Cu_1Cr_3 samples) are found to be $\text{BAS}:\text{LAS}=9.1$ on Cu_2Cr_1 and $\text{BAS}:\text{LAS}=5.0$ on Cu_1Cr_3 respectively. The chromium enriched (Cu_1Cr_3) displayed strong Lewis acidity than the Cu_2Cr_1 . The existence of slightly high LAS on chromium rich Cu_1Cr_3 compared to Cu_2Cr_1 seems to influence the conversion and also the product distribution.

On one hand the copper enriched Cu–Cr–O (Cu_2Cr_1) sample demonstrated 3 times higher conversion (both glycerol and 1,2-PDA) than the chromium rich Cu–Cr–O (Cu_3Cr_1), on the other the selectivity of 2,6-DMP is not affected though the BAS ratios on these samples (Cu_2Cr_1 and Cu_1Cr_3) is $\text{BAS}_{\text{Cu}_2\text{Cr}_1}:\text{BAS}_{\text{Cu}_1\text{Cr}_3}=0.9$; exemplifying that these sites does play significant role in the conversion of glycerol and 1,2-PDA. On the contrary the LAS are almost twice on Cu_1Cr_3 compared to Cu_2Cr_1 indicating that the dehydration of glycerol on Lewis acid sites. The rate of glycerol dehydration seems to be higher on Cu_1Cr_3 and as a result the rate of formation of 2,6-DMP is higher which is probably due to poor dehydrogenation activity of Cu_1Cr_3 compared to the copper rich Cu_2Cr_1 (Table 2). Basicity of the catalyst seems to advocate the selectivity of both 2,6-DMP

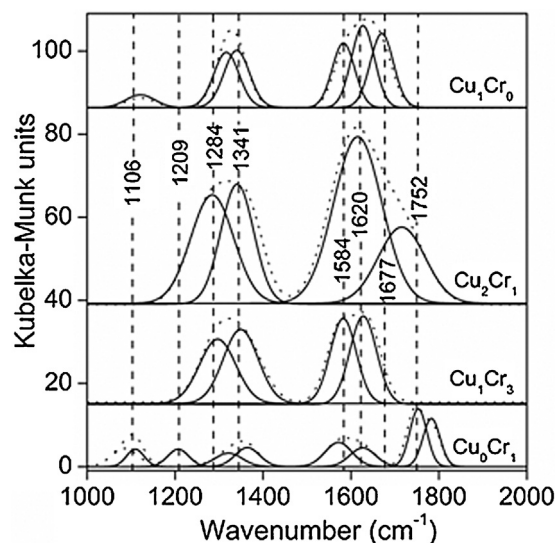
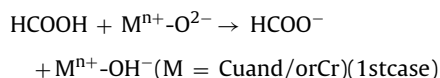


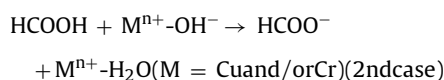
Fig. 7. Formic acid adsorbed on (a) Cu_1Cr_0 (b) Cu_2Cr_1 (c) Cu_1Cr_3 and (d) Cu_0Cr_1 catalysts.

and 6-HMP as the dehydrogenation reaction occurs on basic sites present on the Cu–Cr–O surface.

Hence an insight on the role of surface basicity is examined by formic acid adsorbed in situ by DRIFTS analysis of Cu_1Cr_0 , Cu_0Cr_1 , Cu_1Cr_3 and Cu_2Cr_1 samples (Fig. 7). Due to broad IR signals the spectra were deconvoluted using Gaussian fitting. The DRIFT spectra show IR absorption band at 1677 (shoulder), 1620 , 1427 and 1341 cm^{-1} , which are due to the $\nu(\text{CH})$, $\nu_{\text{as}}(\text{COO})$, $\delta(\text{CH})$ and $\nu_{\text{s}}(\text{COO})$ modes of surface formate groups [44,45]. The strong absorption band at 1620 cm^{-1} is associated with adsorption of formic acid on the catalyst surface. The bands at 1584 and 1677 cm^{-1} are emerged due to decomposition of surface formate species [44]. The band at 1752 cm^{-1} is an indication of formic acid associatively adsorbed on the weak basic sites present on the catalyst surface. A prominent band around 1284 cm^{-1} (present in both Cu_2Cr_1 and Cu_1Cr_3) is probably due to formic acid adsorbed on the CuCr_2O_4 surface. On bulk chromia (Cu_0Cr_1) adsorption of formic acid is weaker than on the copper containing Cu_1Cr_0 , Cu_2Cr_1 and Cu_1Cr_3 samples. The envisaged basic sites on the catalyst surface are O^{2-} and OH^- . Adsorption of formic acid on these sites can be illustrated as follows:



Alternatively, interaction might take place through the following reaction:



The reduced surfaces of the mixed oxides upon exposure to steam at and above 300°C ; usually convert the coordinatively unsaturated $\text{M}^{x+1}\text{O}^{2-}$ ($\text{M} = \text{Zn}$ and/or Cr) species into $\text{HO}^-\text{-M}^{x+}\text{-OH}$ hydroxy groups by dissociative adsorption [8,9,42]. It is unlikely to expect the same from Cu containing mixed oxides ($\text{CuO-CuCr}_2\text{O}_4$) as the metallic copper will not react with steam even at very high temperatures to generate gaseous H_2 and CuO species i.e. $\text{Cu} + \text{H}_2\text{O} \rightleftharpoons \text{CuO} + \text{H}_2$ (reverse reaction of CuO reduction). Evidence to this fact is observed from the H_2O adsorbed DRIFT spectra of both Cu_2Cr_1 and Cu_1Cr_3 samples which did not record a band at 3550 cm^{-1} (Fig. S7) attributed to molecular water

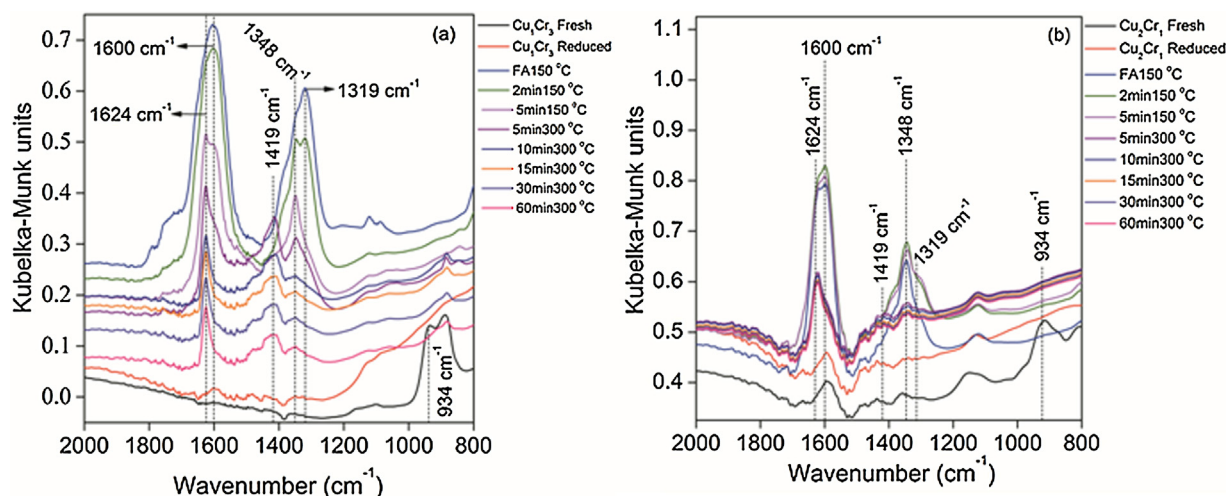


Fig. 8. Formic acid adsorbed at 150 °C over (a) Cu_1Cr_3 and (b) Cu_2Cr_1 samples and the spectra recorded at different intervals of time after subsequent flush in N_2 flow at 150 °C and 300 °C.

($\text{M}^{n+}-\text{H}_2\text{O}$) [44]. Hence the first case may be considered. It has been observed that appearance of high valence Cr^{x+} ($3 < x < 6$) species at a vibrational band of 934 cm^{-1} in the fresh form of $\text{Cu}-\text{Cr}-\text{O}$ samples disappeared after reduction (Fig. S7a & S7b). These high valent Cr species were not regenerated after reduction and subsequent steam exposure (Fig. S7a and S7b). In addition rejection of second possibility is further supported from the formic acid DRIFT spectra that revealed the strong vibrational bands at 1620 cm^{-1} present in both Cu_2Cr_1 and Cu_1Cr_3 samples (Fig. 7). However, the band intensity of 1620 cm^{-1} peak is very strong over Cu_2Cr_1 than on Cu_1Cr_3 although an equimolar dose of formic acid is injected on both samples (Fig. 8a and b). Reduction of surface $\text{Cu}-\text{Cr}-\text{O}$ leads to dehydroxylation of metal oxides to form coordinatively unsaturated O^{2-} ions i.e. basic sites. Therefore the basic sites on the $\text{Cu}-\text{Cr}-\text{O}$ samples are in the form of $\text{M}^{n+}-\text{O}^{2-}$ species which were converted to $\text{M}^{n+}-\text{OH}^-$ by the adsorption of HCOOH (1st case).

The higher number of anion vacancies on chromium rich Cu_1Cr_3 can be anticipated than on Cu_2Cr_1 from the high surface oxygen density on Cu_1Cr_3 sample from the XPS analysis (Table S4). The IR spectra of fresh sample showed a prominent band near 934 cm^{-1} (in both Cu_1Cr_3 and Cu_2Cr_1) due to $\text{Cr}=\text{O}$ species attributed to Cr in higher oxidation >3 and <6 . These species were converted to Cr^{3+} as the vibrational band disappeared after reduction (Fig. 3A and B). Further, the 934 cm^{-1} band is not retained upon reduction and subsequent exposure of the sample to steam at 150 °C and also after out gassing the sample at 300 °C (Fig. 8a and b) thus suggest the stable form of CuCr_2O_4 during the reaction conditions wherein the aqueous glycerol and 1,2-PDA were subjected to $\text{Cu}-\text{Cr}-\text{O}$ even at elevated temperatures. While upon formic acid adsorption, no bands were recorded at *ca.* 3550 cm^{-1} indicating that molecular water is not formed (Fig. 8).

However, the hydroxy groups on the catalyst surface possess Bronsted and Lewis acidity, although they behave as basic $-\text{OH}$ groups, because the bond with which they are coordinated to the metal cation is ionic. Reduction of mixed metal oxides leads to formation of coordinatively unsaturated O^{2-} ions (basic) and an adjacent anion vacancy which exposes coordinated cations (Lewis acid sites) [44]. The sample that possess strong acid sites (Fig. 6) with mild basic sites (Fig. 7) demonstrated more selectivity towards 2,6-DMPip. The basic sites are generated from the surface copper species after reduction. The metallic Cu in close proximity to CuCr_2O_4 species are the desired active sites for the high yield of 2,6-DMP. These results confess that a fine tuning of acid-base sites by surface modification can alter the product distribution particularly

in the synthesis of alkyl hetero aromatics. Finally it can be concluded that selective synthesis of alkyl hetero aromatics by vapour phase dehydrocyclization of glycerol and 1,2-PDA requires a pair of strong basic sites and higher number of surface Cu metal sites for achieving high rate of 2,6-DMP.

5. Conclusions

The $\text{Cu}-\text{Cr}-\text{O}$ catalysts with different mole ratios were prepared and tested for synthesis of 2,6-DMP by dehydrocyclization of aqueous glycerol and 1,2-PDA. The N_2O decomposition measurements concluded that the rate of 2,6-DMP is in good correlation with Cu metal surface area of the catalyst. The results demonstrated that the Cu_2Cr_1 catalyst exhibited the most promising catalytic activity for the synthesis of 2,6-DMP. All Cu-Cr catalysts have shown normal spinel structure except for Cu_1Cr_0 and Cu_0Cr_1 catalysts. Cu_1Cr_3 depicted combined phases of spinel-type CuCr_2O_4 and rhombic Cr_2O_3 . XRD results identified the different phases (CuO , CuCr_2O_4 and Cr_2O_3) in calcined and metallic copper with small intense of CuCr_2O_4 spinel phase as observed in reduced samples. The FT-IR and Raman spectroscopy analyses revealed the structure of copper chromite spinel. The results obtained by XPS and H_2 -TPR are self-consistent supplying arguments for the conclusion that spinels exposed to air, contained surface Cr^{6+} ions, which were easily reduced. The catalytic performance over the reduced sample showed better activity than calcined catalyst emphasizing that both the metallic copper and copper chromite spinel are active for the synthesis of 2,6-DMP. Pyridine and formic acid adsorbed DRIFT spectroscopy indicated clear distinction between Bronsted and Lewis sites. Based on these results it can be concluded that the rate of 2,6-DMP is dependent on strong basic sites on $\text{Cu}-\text{Cr}-\text{O}$ and the copper metal surface area. The catalyst composed of $\text{Cu}/\text{Cr}=2$ could be an optimum in the selective dehydrocyclization of crude bioglycerol obtained from the bio-diesel plant to synthesize an industrially important 2,6-dimethylpyrazine.

Acknowledgements

The authors VK and RS thank CSIR New Delhi for fellowship. Financial support from CSIR New Delhi under INDUS-MAGIC programme CSC-0123 is acknowledged.

Appendix A. Supplementary data

Supplementary data associated with this article can be found, in the online version, at <http://dx.doi.org/10.1016/j.apcatb.2016.04.018>.

References

- [1] T. Miyazawa, Y. Kusunoki, K. Kunimori, K. Tomishige, *J. Catal.* **240** (2006) 213–221.
- [2] Y. Kusunoki, T. Miyazawa, K. Kunimori, K. Tomishige, *Catal. Commun.* **6** (2005) 645–649.
- [3] M.O. Guerrero-Perez, J.M. Rosas, J. Bedia, J. Rodríguez-Mirasol, T. Cordero, *Recent Pat. Chem. Eng.* **2** (2009) 11–21.
- [4] F. Jerome, Y. Pouilloux, J. Barrault, *Chem. Sustainable Chem.* **1** (2008) 586–613.
- [5] A.D. Mohanprasad, P. Kiatsimkul, W.R. Sutterlin, G.J. Suppes, *Appl. Catal. A: Gen.* **281** (2005) 225–231.
- [6] L. Forni, *J. Catal.* **111** (1988) 199–209.
- [7] R. Sarkari, Ch. Anjaneyulu, V. Krishna, R. Kishore, M. Sudhakar, A. Venugopal, *Catal. Commun.* **12** (2011) 1067–1070.
- [8] A. Venugopal, R. Sarkari, C. Anjaneyulu, V. Krishna, M. Kotes Kumar, *Appl. Catal. A* **441–442** (2012) 108–118.
- [9] A. Venugopal, R. Sarkari, Ch. Anjaneyulu, V. Krishna, M. Kotes Kumar, N. Narender, A.H. Padmasri, *Appl. Catal. A* **469** (2014) 398–409.
- [10] A. Venugopal, R. Sarkari, S. Naveen Kumar, M. Kotes Kumar, S. Syed John, J. Krishna Reddy, A.H. Padmasri, *J. Chem. Sci.* **126** (2014) 387–393.
- [11] G.W.H. Cheesman, E.S.G. Werstiuk, *Adv. Heterocycl. Chem.* **14** (1972) 99–209.
- [12] T. Rizk, E.J.F. Bilodeau, A.M. Beauchemin, *Angew. Chem. Int. Ed.* **48** (2009) 8325–8327.
- [13] G. Buchi, J. Galindo, *J. Org. Chem.* **56** (1990) 2605–2606.
- [14] J.J. Brophy, G.W.K. Cavill, *Heterocycles* **14** (1980) 477–504.
- [15] X. Li, C. Xu, C. Liu, N. Zhang, J. You, Q. Wu, *J. Mol. Catal. A* **371** (2013) 104–110.
- [16] V. Krishna, S. Naveen Kumar, S. Reema, A. Hari Padmasri, K.V.R. Chary, A. Venugopal, *Appl. Catal. A* **488** (2014) 275–284.
- [17] L.M. Plyasova, I.Yu. Molina, T.A. Krieger, L.P. Davydova, T.M. Yurieva, *J. Mol. Catal. A* **158** (2000) 331–336.
- [18] O. Ilinich, W. Ruettinger, X. Liu, R. Farrauto, *J. Catal.* **247** (2007) 112–118.
- [19] J. Chen, X. Zhang, H. Arandian, Y. Peng, H. Chang, J. Li, *Catal. Today* **201** (2013) 12–18.
- [20] B. Dragoi, A. Ungureanu, A. Chiriac, V. Hulea, S. Royerc, E. Dumitriu, *Catal. Sci. Technol.* **3** (2013) 2319–2329.
- [21] J. Zuo, C. Xu, B. Hou, C. Wang, Y. Xie, Y. Qian, *J. Raman Spectrosc.* **27** (1996) 921–923.
- [22] C. Liang, Z. Ma, L. Ding, *Catal. Lett.* **130** (2009) 169–176.
- [23] J.F. Xu, W. Ji, Z.X. Shen, W.S. Li, S.H. Tang, X.R. Ye, D.Z. Jia, X.Q. Xin, *J. Raman Spectrosc.* **30** (1999) 413–415.
- [24] K. Premalatha, P.S. Raghavan, B. Viswanathan, *Appl. Catal. A* **419** (2012) 203–209.
- [25] M.J. Climent, A. Corma, P.D. Frutos, S. Iborra, M. Noy, A. Vely, P. Concepcion, *J. Catal.* **269** (2010) 140–149.
- [26] B. Zhao, P. Liu, H. Zhuang, Z. Jiao, T. Fang, W. Xu, B. Lub, Y. Jiang, *J. Mater. Chem. A* **1** (2013) 367–373.
- [27] R.D. Waldron, *Phys. Rev.* **99** (1955) 1727–1735.
- [28] W.B. White, B.A. Deangelis, *Spectrochim. Acta* **25** (1967) 985–993.
- [29] R. Bajaj, M. Sharma, D. Bahadur, *Dalton Trans.* **42** (2013) 6736–6744.
- [30] S.M. El-Sheikh, R.M. Mohamed, O.A. Fouad, *J. Alloy. Compd.* **482** (2009) 302–307.
- [31] M.A. Khafri, M.H.K. Lafdani, *Powd. Technol.* **222** (2012) 152–159.
- [32] D.L. Hoang, A. Dittmar, M. Schneider, A. Trunschke, H. Lieske, K.W. Brzezinka, K. Witke, *Thermochim. Acta* **400** (2003) 153–163.
- [33] J.J. Bravo-Suarez, B. Subramaniam, R.V. Chaudhari, *J. Phys. Chem. C* **116** (2012) 18207–18221.
- [34] S. Rodrigues, K.T. Ranjit, S. Uma, I.N. Martyanov, K.J. Klabunde, *J. Catal.* **230** (2005) 158–165.
- [35] Z. Zhangab, P. Wang, *J. Mater. Chem.* **22** (2012) 2456–2464.
- [36] M. Yin, C.K. Wu, Y. Lou, C. Burda, J.T. Koberstein, Y. Zhu, S. O'Brien, *J. Am. Chem. Soc.* **127** (2005) 9506–9511.
- [37] J. Chena, W. Shia, J. Li, *Catal. Today* **175** (2011) 216–222.
- [38] J. Sloczynski, J. Janas, T. Machej, J. Rynkowski, J. Stoch, *Appl. Catal. B* **24** (2000) 45–60.
- [39] J. Li, X. Liang, S. Xu, J. Hao, *Appl. Catal. B* **90** (2009) 307–312.
- [40] A.L.R. Toro, R. Berenguer, C. Quijada, F. Montilla, E. Morallon, J.L. Vazquez, *J. Phys. Chem.* **110** (2006) 24021–24029.
- [41] J. Zhu, Q. Gao, *Microporous Mesoporous Mater.* **124** (2009) 144–152.
- [42] G. Busca, *Catal. Today* **41** (1998) 191–206.
- [43] M. Thomas, T.B. Balkrishna, N.R. Shiju, G.S. Hegde, S.B. Rao, S.C. Gopinath, *Phys. Chem. Chem. Phys.* **4** (2002) 4260–4267.
- [44] C. Martin, I. Martin, V. Rives, *J. Mol. Catal.* **73** (1992) 51–63.
- [45] J.C. Lavalley, *Catal. Today* **27** (1996) 377–401.